Journal of
Materials Chemistry B

ROYAL SOCIETY
OF CHEMISTRY

PAPER

View Article Online
View Journal | View Issue

Check for updates

Cite this: *J. Mater. Chem. B*, 2025, **13**, 15606

Emissive and photothermal poly(*N*-isopropylacrylamide)-immobilized carbon-nanodots with thermoresponsive drug release properties

Salvatore Petralia, *[abcd] Grazia M. L. Consoli, [bc] Ludovica Maugeri,[a] Nicolò Musso,[de] Corinna Lombardo,[a] Giuseppe Consiglio, [f] Mario Scuderi, [g] Silvia Scalese [g] and Giuseppe Forte *[a]

This study explores the design and synthesis of an innovative thermoresponsive nanocomposite for applications in drug delivery and controlled release. The nanocomposite core consists of carbon dots (CDs), covered by functionalized agarose units tethered to poly(*N*-isopropylacrylamide) (PNM), a thermoresponsive polymer with a lower critical solution temperature (LCST) of approximately 32 °C. Upon irradiation at 405 nm, localized heating within the CD core is efficiently transferred to the PNM shell through agarose linkages, resulting in modulation of the LCST toward physiologically relevant temperatures, optimal for biomedical applications. The structural integrity and composition of the CDs–agar–PNM nanocomposite were confirmed through ATR-FTIR spectroscopy, nuclear magnetic resonance (NMR) spectroscopy and scanning electron microscopy (SEM). Transmission electron microscopy (TEM) revealed the hierarchical structure of the material, showing ∼7 nm primary carbon domains aggregated into compact spherical nanostructures (∼200 nm) after PNM functionalization. Dynamic light scattering (DLS) analyses revealed that the coil-to-globule transition of PNM occurs at temperatures exceeding 34 °C. UV-Vis spectroscopy demonstrated effective loading of curcumin and its temperature-dependent release, with drug release triggered above the LCST threshold. Molecular dynamics (MD) simulations supported the experimental findings and provided additional mechanistic insight into the influence of the PNM chain length. The simulations revealed that longer polymer chains exhibit stronger adsorption onto agarose surfaces, mediated by increased hydrogen bonding, a higher number of intermolecular contacts, and more favorable interaction energies, ultimately resulting in an elevated LCST. The CDs–agar–PNM nanostructures composed of a C-sp^2 inner core and an agarose–PNM outer shell showed good photothermal conversion properties (η = 38.8 ± 2.8%), blue-green photoluminescence yield and low cytotoxicity. Photophysical properties were demonstrated by the photogeneration of Au nanostructures upon 300 nm light exposure, according to the calculated semiconductor band-gap value of 2.45 eV. In summary, the synthesized nanocomposite exhibits enhanced thermal responsiveness, robust photothermal properties, and high structural stability, making it a promising platform for targeted cancer therapy and precision drug delivery applications.

Received 13th August 2025,
Accepted 6th November 2025

DOI: 10.1039/d5tb01844g

rsc.li/materials-b

1. Introduction

Effective drug delivery systems (DDSs) are critical in modern medicine to maintain therapeutic drug concentrations over time, ensuring efficacy and safety. Poor control of drug release can lead to significant problems, including overdosing or incomplete treatment, which highlight the importance of precision in DDS development.[1] Strategies for targeted drug

---

[a] Department of Drug and Health Sciences, University of Catania, Via Santa Sofia 64, 95125 Catania, Italy. E-mail: salvatore.petralia@unict.it, gforte@unict.it

[b] Consiglio Nazionale delle Ricerche-Istituto di Chimica Biomolecolare, Via Paolo Gaifami 18, 95126 Catania, Italy

[c] CIB-Interuniversity Consortium for Biotechnologies U.O. of Catania, Via Flavia, 23/1, 34148 Trieste, Italy

[d] Advanced and Innovative Diagnostic Academy (A.I.D.A.) S.r.l., Spin-off of BRIT Research Center, University of Catania, 95125 Catania, Italy. E-mail: spinoffaida@gmail.com

[e] Faculty of Medicine and Surgery, "Kore" University of Enna, Contrada Santa Panasia, 94100 Enna, Italy

[f] Department of Chemical Science, University of Catania, Via Santa Sofia 64, 95125 Catania, Italy

[g] Consiglio Nazionale delle Ricerche-Istituto per la Microelettronica e Microsistemi (CNR-IMM), Ottava Strada n. 5, I-95121 Catania, Italy

delivery include passive targeting, active targeting, and the use of external stimuli such as temperature, pH, magnetic fields, and ultrasound. Nanocarriers like liposomes, polymeric nanoparticles, nanocapsules, and hydrogels are widely used in these approaches due to their ability to deliver drugs to specific sites in a controlled manner.[2–5] Among these, polymer-based hydrogels have emerged as highly promising candidates due to their biocompatibility, versatility, and tunable physicochemical properties. Hydrogels are hydrophilic polymer networks capable of absorbing large amounts of water without dissolving, maintaining their structure under physiological conditions.[6] Particularly notable are "smart" hydrogels, which can respond to external stimuli such as temperature, pH, and electric fields by undergoing structural and volumetric changes.[6,7] Thermoresponsive hydrogels based on poly(*N*-isopropylacrylamide) (PNM) are among the most studied due to their reversible phase transitions near physiological temperatures. PNM exhibits a lower critical solution temperature (LCST) of ~32 °C, below which the polymer is hydrated and forms random coils and above which it collapses into compact globules.[8–11] This thermal responsiveness allows PNM-based hydrogels to swell and shrink in response to temperature changes, enabling controlled drug release.[11–14] Despite its widespread use, the LCST of PNM of ~32 °C is slightly below body temperature, which can limit its effectiveness for certain biomedical applications. Therefore, research has focused on modifying the structure of PNM to raise the LCST above 37 °C and enhance its biocompatibility and biodegradability. One approach involves copolymerization with hydrophilic comonomers such as *N*,*N*-diethylacrylamide (DEA) and *N*,*N*-dimethylacrylamide (DMA).[15,16] Random and block copolymers of PNM with these monomers have demonstrated significant LCST increases, expanding their applicability. Stereo complexation, which leverages interactions between enantiomeric polymers, has also been shown to raise the LCST. For instance, triblock copolymers of PNM and poly(L-lactic acid) (PLA) have achieved LCSTs of up to 38.5 °C through optimal stereocomplexation.[17] Additionally, altering the tacticity of PNM offers another method to tune its LCST. De Oliviera *et al.*, using molecular dynamics simulations, have demonstrated that LCST values follow the order of syndiotactic > atactic > isotactic PNM.[18] Incorporating acrylamide (Am) monomers into polymer backbones further enhances LCST values, with an Am content of 9–19%, resulting in LCST increases of up to 20 K.[18] Environmental factors, such as pH, also play a role in modulating PNM's thermal response. Copolymers of PNM with propylacrylic acid (PAA) exhibited an LCST shift from 28 °C to 45 °C when the pH increased from 5.0 to 7.0, driven by ionization of the PAA units and subsequent changes in hydrophilicity.[19] While PNM is a widely studied synthetic polymer, concerns about its biodegradability and biocompatibility remain. To address these limitations, functionalization has been explored. The incorporation of star-shaped PCL–COOH improved the biocompatibility, mechanical stiffness, and drug retention of PNM hydrogels while maintaining their thermoresponsive behavior. These hydrogels, formed *via* frontal polymerization, demonstrated low cytotoxicity and suitability for controlled drug delivery.[20] PNM–CNC hydrogels, prepared through simple mixing without additional cross-linkers, exhibited enhanced fibroblast compatibility and thermo-responsive control of cell behavior. Their optimized stiffness and porosity make them promising for 3D cell culture and 3D printing applications.[21] A thermosensitive PNM–chitosan hydrogel supported cell encapsulation, survival, and proliferation. Functionalized with collagen/chitosan microspheres, it showed potential for application in regenerative medicine and cell therapy.[22] Hybrid PNM nanosystems functionalized with magnetic nanoparticles enabled controlled delivery of 5-fluorouracil and oxaliplatin. These biocompatible systems reduced colon cancer cell proliferation by 57%, offering a promising platform for cancer therapy.[23] The natural compound agarose, an FDA-approved natural polysaccharide, forms porous gel structures in water by utilizing noncovalent interactions such as hydrogen bonds and electrostatic attractions, making it an ideal candidate for enhancing PNM properties.[24,25] Agarose-based hydrogels exhibit excellent drug delivery potential due to their biocompatibility and ability to be crosslinked *via* non-covalent interactions.[26] Functionalizing PNM with agarose improves the biocompatibility and biodegradability of the hydrogel, while also maintaining its thermal responsiveness.[27,28]

Carbon-based nanostructures, including carbon nanodots (CDs), are a captivating class of materials, manifesting intriguing photophysical properties, such as photoluminescence, photothermal effects, and semiconductor properties.[29,30] The photothermal mechanism of CDs is mainly based on the non-radiative process from the LUMO to the HOMO, which results in photothermal conversion efficiency (η) values ranging from 20% to 50%. Nevertheless, the lower η and the lower excitation wavelength in the range of 400–550 nm (compared to the gold nanostructures with $\eta > 50\%$ and excitation above 550 nm), their photoluminescence, semiconductor properties and low toxicity permit applications in bioimaging and combined photothermal–photodynamic therapy.[31] Our research explored PNM through experimental and computational methods. Molecular dynamics showed that hydroxyl-rich hydrophilic surfaces stabilize its coil form, raising the transition temperature.[32] We synthesized carbon polymer dots with PNM cross-links, exhibiting strong photothermal properties and efficient drug release under irradiation.[33–35] Nanohybrids combining graphene oxide, gold nanoparticles, and PNM enabled dual photo-induced hyperthermia and drug release at 680 nm, while titania–gold–PNM systems integrated photothermal effects (532 nm), thermoresponsive behavior, and photocatalysis.[36,37] This study focuses on enhancing the biocompatibility of PNM while raising its LCST for hyperthermia-controlled drug delivery applications. We developed a nanocomposite composed of CDs, agarose, and PNM, leveraging the hydrophilic structure of agarose to modulate PNM's thermal properties and achieve the desired phase transition temperature. Our research includes the synthesis, characterization, and thermal analysis of this novel three-component system, where CDs form a core surrounded by an agarose shell, further functionalized with PNM (Scheme 1). The nanocomposite was prepared through a multistep approach, as shown in Scheme 1A. Molecular dynamics

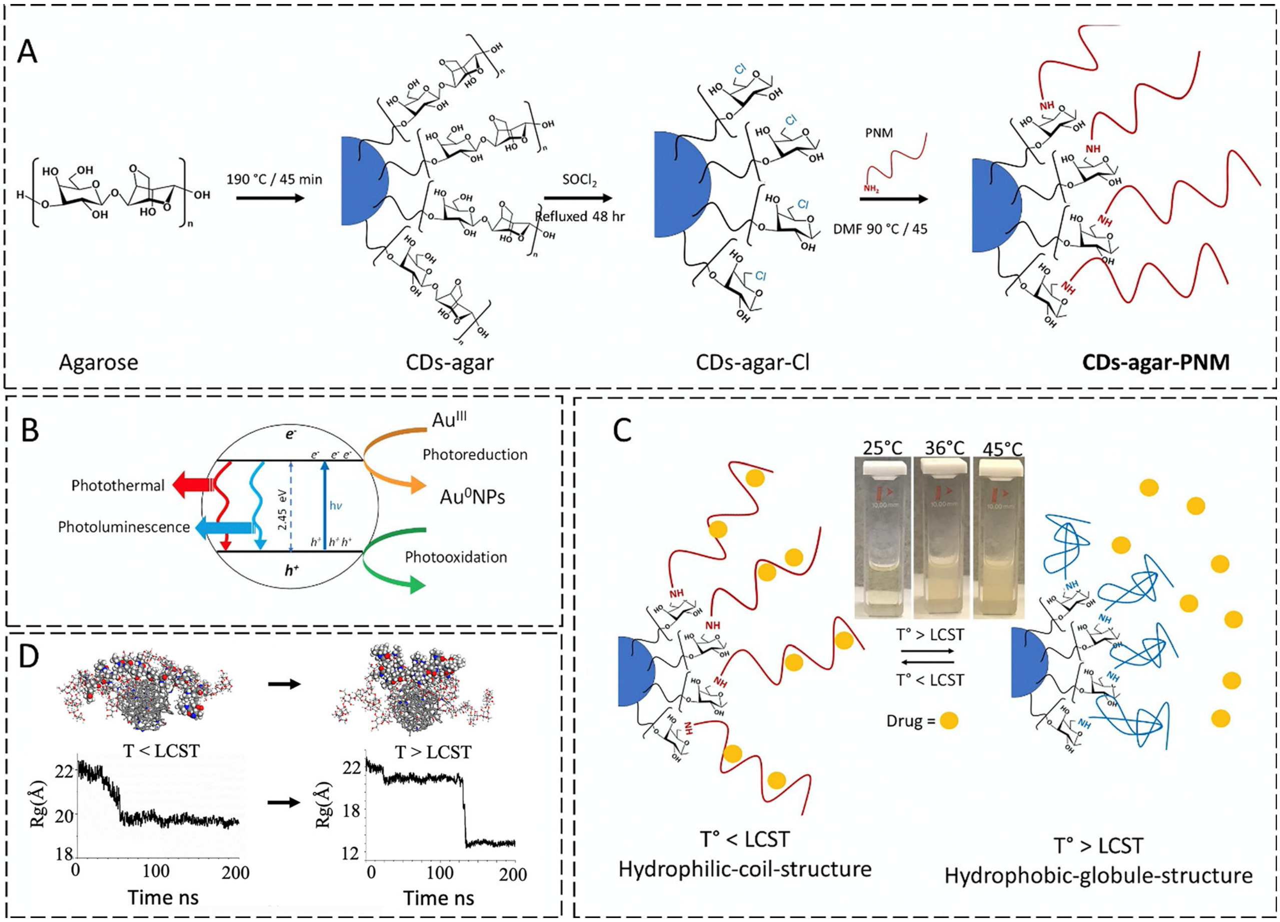

Scheme 1 Schematic illustration of the (A) preparation of the CDs–agar–PNM nanocomposites, (B) photophysical properties of CDs–agar–PNM nanocomposites (the inset shows representative thermographs during photothermal experiments) and (C) thermo-responsive drug-release properties (the inset shows the representative photographs of the sample at different temperatures) and (D) modelling simulation of the radius of gyration at 305 K and 310 K of CDs–agar–PNM.

simulations were conducted to elucidate the interaction mechanism between the polymer and agarose in support of the experimental data. Additionally, the computational study aimed at predicting whether increasing the polymer length relative to the size of agarose (PNM/agarose ratio) leads to an increase in LCST and at quantifying its tuning effect. The results confirm successful adjustment of the LCST to body temperature, demonstrating the material's potential for targeted hyperthermia treatments and controlled drug release; furthermore, they suggest that increasing the polymer length relative to the size of agarose leads to an increase in the transition temperature. This innovative nanocomposite represents a promising platform for precision drug delivery in biomedical applications.

2. Methods and materials

2.1 Chemicals and instrumentation

All reagents including amine terminated poly(*N*-isopropylacrylamide) (5500 Da) and agarose were purchased from Merck and used as received. Optical absorption UV-vis spectra were recorded on a PerkinElmer 365 spectrophotometer. Photoluminescence (PL) spectra at different excitation wavelengths were measured using a HORIBA spectrofluorometer. A quartz cuvette with an optical length of 10 mm was used.

2.2 CDs–agar–PNM preparation

The CDs–agar–PNM nanocomposites were prepared using the approach depicted in Fig. 1. Firstly, 200 mg of agarose was pyrolyzed for 45 min at 190 °C to obtain a carbon-nanodot material. The dark-reddish solid was washed with 1 mL of Milli-Q water to eliminate the excess of reagent and by-products and finally sonicated for 2 min. The dispersion was separated by centrifugation (8000 rpm, 15 min) and the red-yellowish supernatant of CDs–agar was filtered (0.2 μm pore size) and further purified by dialysis using Milli-Q water through a dialysis membrane (10 kDa cutoff) for 46 h. The purified sample was lyophilized at −20 °C. Secondly, 11 mg of CDs–agar was refluxed in SOCl$_2$ (20 mL) for 48 h to obtain the chloro derivative CDs–agar–CH$_2$Cl. The excess of SOCl$_2$ and the by-products were removed by evaporation. Then, the solid product was resuspended in 2 mL of DMF (dimethylformamide) and

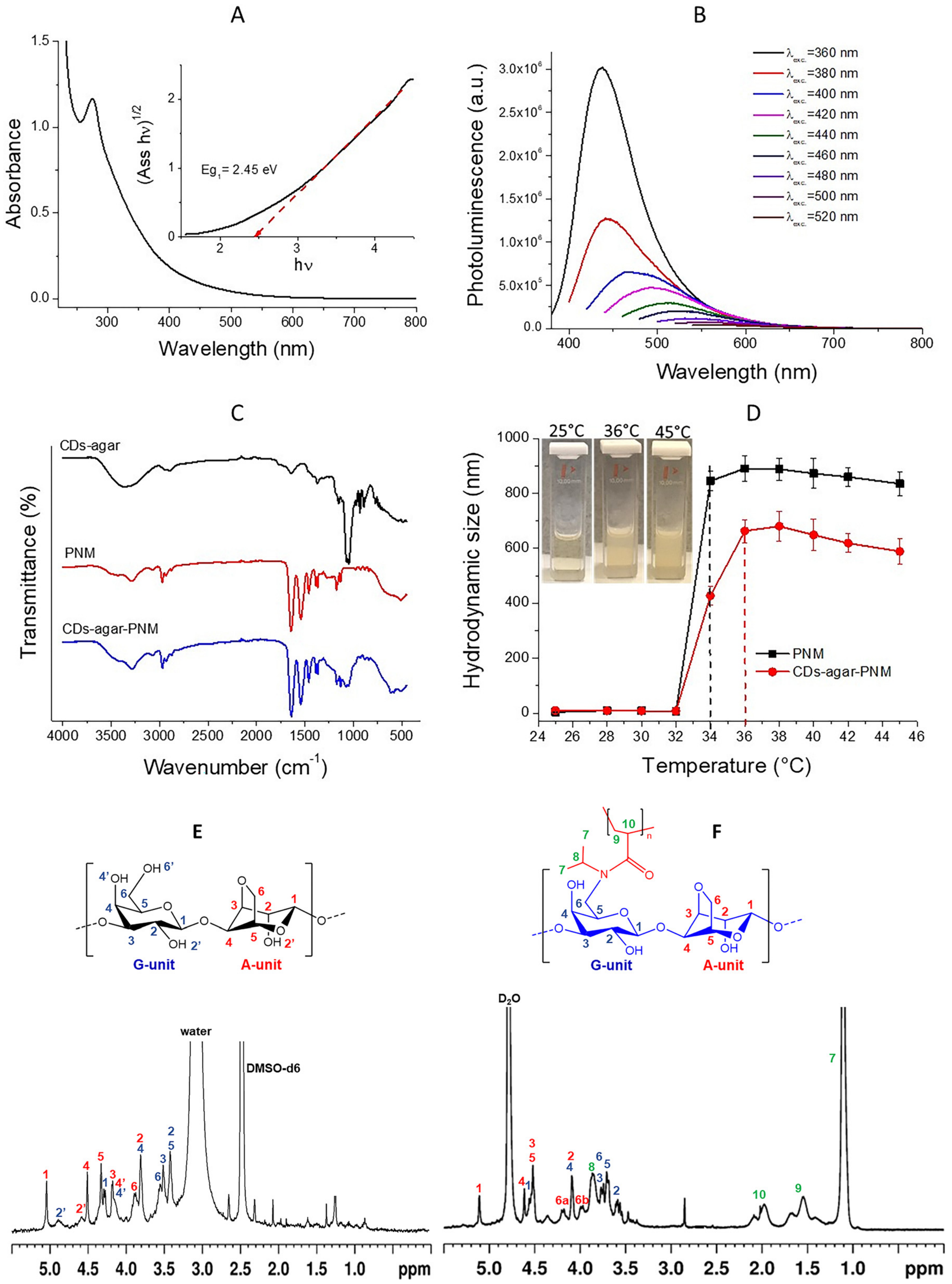

Fig. 1 CD–agar–PNM: (A) optical absorption spectrum of CDs–agar–PNM (1 mg mL^{-1}) dispersions in water, with the inset showing Tauc plot for the optical band gap evaluation of CDs–agar–PNM; (B) fluorescence spectrum of CDs–agar–PNM in water at various excitation wavelengths; (C) ATR-FTIR spectra of CDs–agar (black line), the PNM precursor (red line) and CDs–agar–PNM (blue line); (D) DLS measurements of CDs–agar–PNM (red line) and PNM precursor (black line) at various temperatures, with the inset showing representative photographs of CDs–agar–PNM water dispersion at 25 °C, 36 °C, and 45 °C; (E) ^{1}H NMR spectrum of CDs–agar in DMSO-*d*6 at 70 °C; and (F) ^{1}H NMR spectrum of CDs–agar–PNM in D_2O at 25 °C.

50 mg of amine terminated PNM was added. The mixture was heated for 24 hours at 100 °C under continuous stirring. After solvent evaporation, the CDs–agar–PNM was purified by filtration (0.2 μm pore size) and by two dialysis processes, using Milli-Q water through dialysis membranes with cutoffs of 20 kDa and 3.5 kDa, both for 46 hours.

2.3 Scanning electron microscopy (SEM)

Morphological characterization of particles was carried out using a field emission SEM (Supra 35 FE-SEM by Zeiss, Oberkochen, Germany), equipped with an EDX microanalysis system (X-Max, 80 mm^2 by Oxford Instruments, Abingdon, UK). Morphological analysis was performed using an in-lens detector, a working distance of 3 mm and a beam energy of 3 keV, while EDX analysis was performed using a beam energy of 15 keV.

2.4 Transmission electron microscopy (TEM)

Transmission electron microscopy (TEM) analyses were carried out using a JEOL JEM-2010F microscope operating at an accelerating voltage of 200 kV in conventional TEM mode. Bright-field (BF) TEM images were acquired to investigate the structural morphology of both samples, namely, the precursor and the final nanocomposite. The samples were prepared by drop-casting aqueous dispersions onto lacey carbon-coated copper grids and allowing them to dry under ambient conditions. All images were recorded at a low electron dose to minimize beam-induced modifications, particularly in the polymeric components of the nanocomposite.

2.5 Nuclear magnetic resonance (NMR)

NMR spectra were recorded on a Bruker Avance 400™ spectrometer (Bruker, Germany), and the chemical shift (δ) was reported in parts per million (ppm) referring to the residual solvent signal (DMSO-d_6, 2.49 ppm and 39.5 ppm, HOD, 4.7 ppm). All NMR spectra were processed using TopSpin 3.0 software by Bruker.

2.6 Dynamic light scattering (DLS) measurements

Dynamic light scattering measurements were performed on a ZetaSizer Nano ZS90 Malvern Instrument (U.K.), equipped with a 633 nm laser, at a scattering angle of 90° and different temperatures (range: 25–45 °C). The size of the particles was calculated from the diffusion coefficient by using the Stokes–Einstein equation.

2.7 Photothermal measurements

The photothermal properties of CDs–agar–PNM were investigated by irradiating a glass tube (diameter 3 mm) containing various amounts of CDs–agar–PNM dispersion. A volume of 100 μL of the CDs–agar–PNM dispersion was irradiated with a CW laser at 405 nm (different laser powers) for various durations. We used a FLIR infrared thermal imaging camera to measure the temperature of the solution every 20 s, during the heating and cooling processes.

2.8 Photoreduction experiments (Au-nanostructure formation)

To an aliquot of 2 mL of CDs–agar–PNM (0.5 mg ml^{-1}) in water was added a volume of 20 μL of $HAuCl_4$ (1.6×10^{-2} M), and after degassing in argon for 15 min, the sample was irradiated in a photoreactor equipped with 2 lamps (300 nm, 16 W) The formation of Au-nanostructures was investigated and confirmed by optical absorption UV-vis spectra. All experiments were replicated three times.

2.9 Curcumin loading

To an aqueous solution of CDs–agar–PNM (1 mg mL^{-1}), an excess of curcumin was added, and the mixture was stirred at 25 °C in the dark for 48 hours. The sample was purified by centrifugation at 13 000 rpm for 5 min. The amount of curcumin entrapped in the carbon dots was measured by the optical absorption at 433 nm in water (ε = 55.000 L mol^{-1} cm^{-1}). The drug loading capacity (LC, %) was calculated using the following equation:

$$\mathrm{LC}\ (\%) = \frac{\text{mg drug in}}{\text{mg drug in} + \text{mg CDs} - \text{agar} - \text{PNM}}$$

2.10 Cytotoxicity test

To evaluate the biocompatibility of the CDs–agar–PNM nanostructures, MTT ([3-(4,5-dimethylthiazol-2-yl)-2,5-diphenyltetrazolium bromide]) assay was performed as previously described.[38] Human colorectal adenocarcinoma cells (CaCo-2 HTB-37™; American Type Culture Collection, Manassas, VA, USA) were grown in Dulbecco's MEM (DMEM) with 10% heat-inactivated fetal bovine serum, 2 mM L-alanyl-L-glutamine, and penicillin–streptomycin (50 units, 50 μg mL^{-1}) and incubated at 37 °C in a humidified atmosphere of 5% CO_2 and 95% air. CaCo-2 cells were plated in 96-well plates and incubated at 37 °C. Different concentrations of nanostructures were tested: 400 μg μL^{-1}, 40 μg μL^{-1}, 4 μg μL^{-1}, 0.4 μg μL^{-1}, 0.04 μg μL^{-1}, and 0.004 μg μL^{-1}. Untreated cells were used as controls. Microplates were incubated at 37 °C in a humidified atmosphere of 5% CO_2 and 95% air, and cytotoxicity was measured after 24 hours. The results of viability were read on a BioTek Synergy H1 modular multimode microplate reader (Agilent, Santa Clara, CA 95051) using a wavelength of 569 nm. Each value was an average of 8 wells. Statistical analysis was performed using the two-stage linear step-up procedure of Benjamini, Krieger and Yekutieli and GraphPad Prism 10 software (Table S1).

2.11 Molecular dynamics setup

The models used in this study were built using BIOVIA Discovery Studio; specifically, the agarose structure was generated starting from the disaccharide agarobiose, which was replicated using the build polymer tools setting the chain length to 8 and the number chain to 2, resulting in a length of 8.43 nm. A spherical carbon core[39] was then covalently bonded to the oxygen atom at position 3 of the galactose unit in agarose.

Additionally, the hydroxyl group (–OH) at position 1 of the 3,6-anhydro-L-galactopyranose unit of agarose was replaced with an amino group (–NH), which was subsequently bonded to the terminal carbon atom of PNM polymers of 24, 32 and 40 monomer units. The use of these three different polymer lengths allowed for a detailed investigation of the effect of increasing the PNM/agarose ratio on the transition temperature. The resulting systems, hereafter referred to as CDs–agar–PNM-24, CDs–agar–PNM-32 and CDs–agar–PNM-40, see Fig. S1, were placed in a box of 10 × 5 × 5 nm, solvated with explicit water molecules and equilibrated through a multi-step procedure. This included an initial energy minimization of 25 000 steps using the steepest descent algorithm, followed by a 10 ns pre-equilibrium molecular dynamics run. Subsequently, 200 ns of production MD simulation was carried out, during which atomic coordinates were stored for further analysis. Simulations were performed at 305 K, 310 K and 315 K, all above the LCST of free PNM. Periodic boundary conditions were applied, and simulations were carried out in the NPT ensemble at a pressure of 1 atm and regulated using a Berendsen barostat, employing the polymer consistent force field (PCFF) provided in the Material Studio package. Additionally, a PCFF water model, known for its good agreement with experimental data, was chosen.[40–44] A time step of 1 fs was used to integrate the equation of motion and the Ewald summation method was employed to take into account long-range electrostatic interactions. To ensure statistical reliability, three independent MD simulations were performed for each system, initialized with different random velocity seeds and run under identical conditions, and the results presented represent average values obtained from these three trajectories. To assess the structural stability, root mean square deviations (RMSDs) of the trajectories with respect to the initial structures were calculated as follows:

$$\mathrm{RMSD}(t) = \sqrt{\frac{1}{N}\sum_{k=1}^{N}\left(r_k(t) - r_k^{\mathrm{init}}\right)^2}$$

where N represents the number of atoms and $r_k(t)$ and r_k^{init} are the instantaneous and the initial coordinates of atom k, respectively. The structural evolution of the polymer was investigated by analyzing the radius of gyration R_g, which is defined as the RMSD of the atoms in a molecule from their common center of mass:

$$R_g = \sqrt{\frac{\sum_{k=1}^{N} m_k d_k^2}{\sum_{k=1}^{N} m_k}}$$

where N is the total number of atoms and d_k is the distance of atom k with mass m_k from the center of mass. The kinetics of hydrogen-bond breaking and formation between the acceptor groups of PNM (O═C—) and hydrogen atoms of the –OH groups on the agarose were investigated using the Luzar and Chandler model,[44] which describes H-bond kinetics through the intermittent hydrogen bond time correlation function, $c(t)$, defined as follows:

$$c(t) = \frac{\langle h(0)|h(t)\rangle}{\langle h\rangle}$$

$c(t)$ is the probability that a hydrogen bond formed at time zero is still intact at the generic time t; $\langle h\rangle$ represents the time average of h; $h(t)$ is a hydrogen-bond population operator that equals 1 if the hydrogen bond is present at time t, and 0 otherwise. Finally, the following geometric criteria were employed to define a hydrogen bond: (a) the hydrogen–acceptor distance <2.5 Å and (b) the donor–hydrogen–acceptor angle $>100°$.

3. Results and discussion

3.1 CDs–agar–PNM preparation and characterization

The nanostructured CDs–agar–PNM nanocomposites were prepared by using the multi-step procedure depicted in Scheme 1A. An innovative method recently developed in our laboratories[33,35] provided the CDs–agar precursor by simple heating of agarose at 190 °C for 45 min in air. This step was carried out without using solvents, oxidizing agents, acids, and instrumentation currently used for the preparation of CDs. The –CH_2OH groups of the precursor CDs–agar were chlorinated to give the intermediate CDs–agar–Cl which by reaction with the amine terminated PNM in DMF provided the final product CDs–agar–PNM.

The UV-vis optical absorption spectra of CDs–agar–PNM exhibited the typical absorption bands for carbon-nanodots. The spectra showed a band centred at 275 nm referred to as $\pi \rightarrow \pi^*$ transition which originates from sp^2 carbon and a lower and broad band centred at about 360 nm, related to the $n \rightarrow \pi^*$ transition generated from C═C and C═O bonds (Fig. 1A). The optical band gap was calculated using Tauc plot, which showed the variation of $(\mathrm{Abs}\ h\upsilon)^{1/2}$ *versus* $(h\upsilon)$ for CDs–agar–PNM (Fig. 1A, inset). The optical energy band gap for the direct allowed transitions was estimated to be about E_g = 2.45 eV. This is in good agreement with carbonaceous nanodots reported in the literature.[33] Fig. 1B depicts the photoluminescence emission spectrum of CDs–agar–PNM at various excitation wavelengths from 360 to 520 nm. Noteworthily, with increasing excitation wavelength, the CDs–agar–PNM water dispersion showed an excitation-dependent emission typical for carbon-based dots. The effective nanocomposite formation was well supported by ATR-FTIR spectra (Fig. 1C), showing the diagnostic peaks of PNM at 3283.3 cm^{-1} (N–H stretching), 2968.2 cm^{-1} (C–H stretching), 1638.8 cm^{-1} (C═O stretching, amide I), 1541.8 cm^{-1} (C═O stretching, amide II), 1375.5 cm^{-1} (C–H bending), and 1132.2 cm^{-1} (C–C stretching). The spectra also show signals characteristic of agarose at 3363.3 cm^{-1} (O–H, stretching), 1367.8 cm^{-1} (C–C bending), 1048 cm^{-1} (C–O stretching), 1068 cm^{-1} and 932.7 cm^{-1} (glycosidic bond stretching), and 892.1 cm^{-1} (C–O–C bridge stretching).

Solution NMR spectroscopy is a technique used to identify the structure of the CD surface and establish whether the precursor suffers any chemical alterations during carbonization.[45] The ^{1}H NMR spectrum clearly showed the presence of a shell of agarose in CDs–agar, Fig. 1E. Sharper signals were observed for DMSO-d6 rather than D_2O as a solvent, Fig. S2, consistent with the low solubility of agarose in water. The assignments of the proton and carbon signals of the β-D-galacto-pyranose (G) and 3,6-anhydro-α-L-galactopyranose (A) residues forming the agarose structure are shown in Fig. 1E and Fig. S3, respectively, and listed (δ, ppm) in Table S2 and Fig. S4.

The functionalization of the CDs–agar with PNM moieties resulted in an improved water-solubility of the CDs, consistent with the good solubility of the PNM in water. The occurred functionalization was evident in the NMR proton spectra, Fig. 1F, 2D-COSY NMR spectra, Fig. S5 and carbon spectra, Fig. S6, of the CDs–agar–PNM, recorded in D_2O. The characteristic proton and carbon resonances of the PNM moieties were detected at 1.07, 1.54, 1.97, and 3.74 ppm (^{1}H) and at 21.09, 31.07, 41.36, 59.9, and 174.9 ppm (^{13}C), corresponding to the CH_3, CH_2, CH–CO, NCH, and carbonyl (C═O) groups, respectively. The typical proton and carbon signals of the PNM moieties were observed at 1.07, 1.54, 1.97, 3.74 ppm and 21.09, 31.07, 41.36, 59.9, 174.9 ppm for the CH_3, CH_2, CH–CO, NCH, and carbonyl (C═O) groups, respectively.

The NMR spectra evidenced no significant chemical alteration of the agarose precursor forming the shell during the CD formation, such as opening of the sugar ring, analogous to what was previously reported for glucose-derived CDs.[30] No NMR signals that could be attributed to the nanoparticle core were observed. This result is compatible with the proposed complete carbonization procedure of the core and the NMR spectroscopy in solution as a technique providing information on the CD shell.[45]

3.2 Scanning electron microscopy (SEM) and transmission electron microscopy (TEM) analyses

The morphology and size of the nanostructures were investigated by SEM and TEM. SEM analysis of the CDs–agar precursor revealed spherical features with apparent diameters between 20 and 80 nm (Fig. 2A). These nanostructures appear as loosely aggregated domains, suggesting partial association of smaller entities.

In the case of the CDs–agar–PNM nanocomposite, SEM micrographs displayed spherical nanostructures with diameters ranging from 200 to 400 nm (Fig. 2B). The larger and more compact morphology indicates that polymer functionalisation promotes the aggregation of the precursor units into stable hybrid nanoparticles.

TEM investigations provided higher-resolution insight into the actual morphology of both systems (Fig. 3). For the CDs–agar sample, TEM images (Fig. 3A) revealed the presence of small, nearly spherical nanoparticles with an average diameter of approximately 7 nm. These nanoparticles tend to assemble into clusters, which correspond to the larger spherical features observed by SEM. This result demonstrates that the entities seen in SEM are not single nanoparticles but aggregates of smaller carbon-based domains.

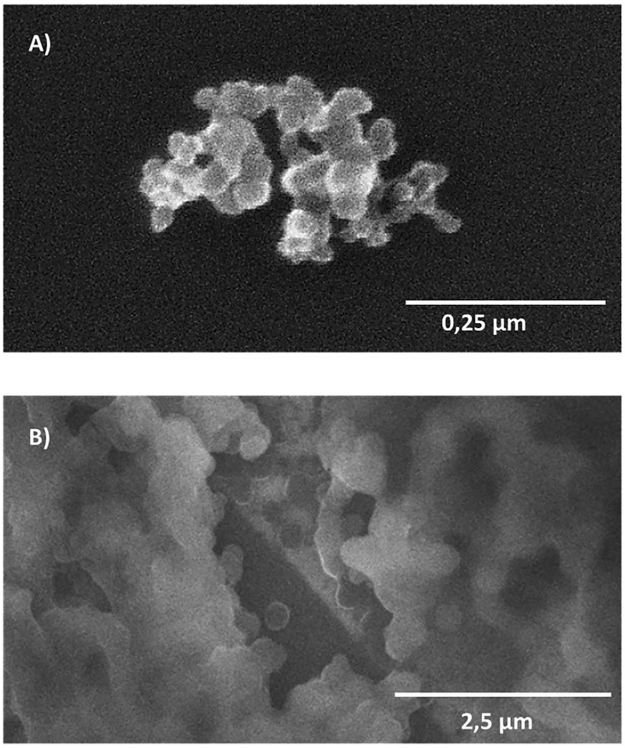

Fig. 2 SEM micrographs of (A) CDs–agar and (B) CDs–agar–PNM nanostructures. The CDs–agar sample shows aggregates of spherical entities with apparent diameters between 20 and 80 nm, while the CDs–agar–PNM nanocomposite exhibits compact spherical structures ranging from 200 to 400 nm.

For the CDs–agar–PNM nanocomposite, TEM micrographs (Fig. 3B) showed well-defined spherical structures with an average diameter of about 200 nm, in good agreement with the SEM results. The morphology appears to be more compact and homogeneous, consistent with the expected incorporation of the CDs–agar units within the polymeric matrix.

These TEM findings also clarify the apparent discrepancy between DLS and SEM measurements. The larger hydrodynamic diameters obtained using DLS for the CDs–agar precursor arise not only from hydration and thermal effects in aqueous suspension but also from the presence of pre-formed aggregates of primary nanoparticles.

Furthermore, energy-dispersive X-ray spectroscopy (EDX) corroborated the successful immobilisation of PNM on the CDs–agar nanostructures. The detection of nitrogen (9.8 wt%) confirmed the presence of the polymeric component, with an average composition of C 80.0 wt%, O 10.2 wt% and N 9.8 wt% for CDs–agar–PNM, compared to C 98.2 wt% and O 1.8 wt% for CDs–agar (average over twenty samples; Si excluded from quantification). The corresponding EDX map for a representative CDs–agar–PNM sample is presented in Fig. S7.

3.3 Dynamic light scattering

The thermo-responsive properties of CDs–agar–PNM were investigated by DLS analysis performed at different temperatures: 25, 28, 30, 32, 34, 36, 38, 40, 42, and 45 °C. In particular,

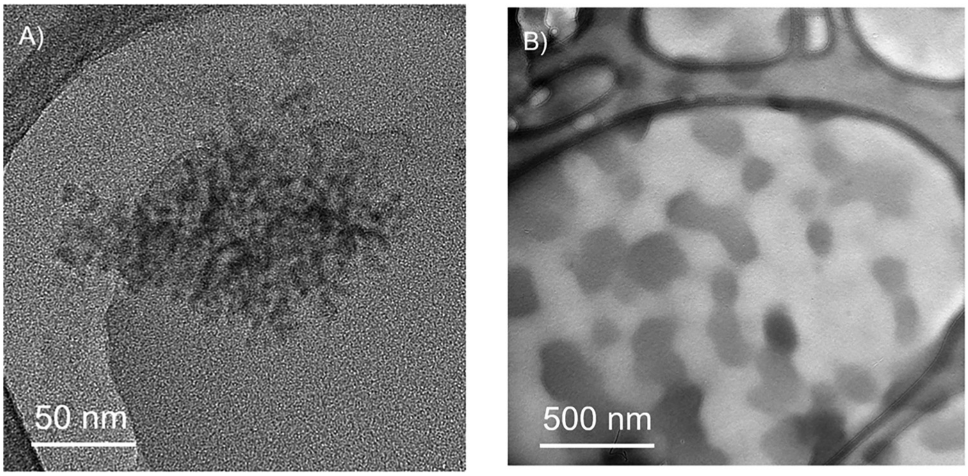

Fig. 3 TEM micrographs of (A) CDs–agar and (B) CDs–agar–PNM nanostructures. In the CDs–agar sample, primary nanoparticles with an average diameter of approximately 7 nm are visible, forming loose clusters. The CDs–agar–PNM nanocomposite displays well-defined spherical structures with an average diameter of about 200 nm, in agreement with SEM observations.

the DLS measurements evidenced that CDs–agar–PNM (2 mg ml^{-1}) in water dispersion (pH = 7) have a mean hydrodynamic diameter around 7–10 nm at temperatures in the range of 25–32 °C. According to the coil-to-globule transition, as the temperature increases, a concurrent increase of the hydrodynamic size occurs, reaching the maximum value of 680.5 ± 55 nm at a temperature of 36 °C. As reported in the literature, during the coil-to-globule transition, water molecules are expelled from the PNM chain (coil-conformation), the amount of hydrogen bonds decreases and the hydrophobicity drastically increases (globule-conformation), resulting in the CDs–agar–PNM structure aggregation (Fig. 1D, black line). For comparison, DLS measurements were also performed on the aqueous solution of the precursor PNM (2 mg ml^{-1}, pH 7.0). In this case, a mean hydrodynamic diameter of 4–6 nm was recorded at temperatures in the range of 25–32 °C. The coil-to-globule transition was completed at a temperature above 34 °C and aggregates with a mean hydrodynamic diameter of around 880 nm were formed (Fig. 1D, red line). The reported experiments show that the LCST value of the CDs–agar–PNM compared to the LCST value of the PNM precursor increases by about 2 °C. This difference is attributable to the presence of the agarose inner shell whose hydrodynamic dimension is temperature-dependent as confirmed by DLS measurements performed on the CDs–agar nanostructure under the same experimental conditions, see Fig. S8. In detail, the hydrodynamic sizes of CDs–agar decrease from about 1910 nm (due to aggregates) to about 200 nm as the temperature rises from 25 °C to 45 °C.

3.4 Photothermal experiments

To investigate the photothermal properties of the CDs–agar–PNM, an aqueous dispersion of product (2 mg ml^{-1}, 100 µL, Abs$_{405\text{nm}}$ = 0.336) was continuously exposed to a 405 nm laser source. The temperature changes were monitored using a standard thermocamera. Fig. 4 illustrates the representative photothermal cycles of the CDs–agar–PNM sample during photothermal experiments. When the temperature of the

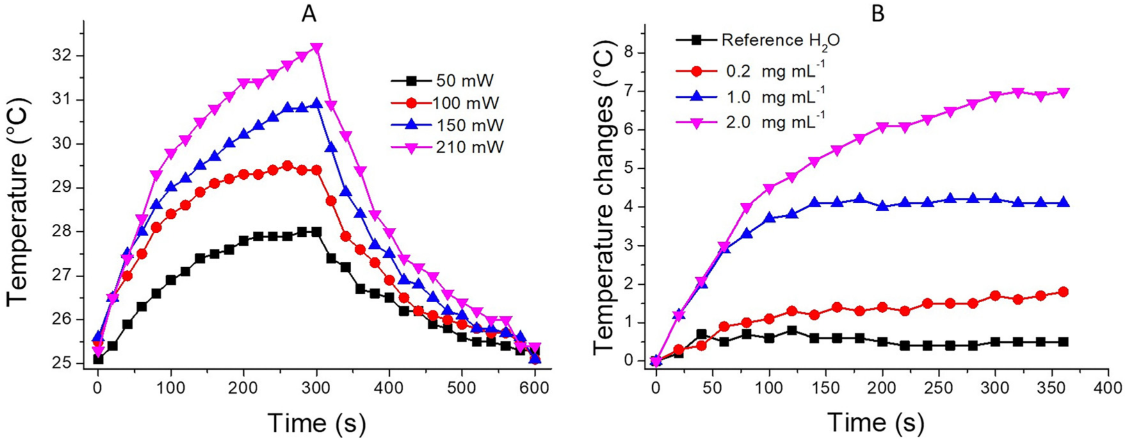

Fig. 4 CDs–agar–PNM photothermal experiments: increase of the temperature values over time for an aqueous dispersion of CDs–agar–PNM (2 mg mL^{-1}, 100 µL, Abs$_{405\text{nm}}$ = 0.33) at (A) different laser powers and (B) different CDs–agar–PNM amounts of 0, 0.2, 1 and 2 mg mL^{-1} (laser power 210 mW).

system reached the maximum value ($T_{\max}$), the laser was switched off and the temperature dropped to environmental temperature ($T_{\text{env.}}$). The power-dependent behaviour was confirmed by experiments performed at different laser powers of 50, 100, 150 and 210 mW, and the temperature values recorded were about 28, 29.4, 39.1, and 32.1 °C, respectively, Fig. 4A. Moreover, to better investigate the correlation between the photothermal effect and the amount of CDs–agar–PNM, experiments were performed using sample dispersions with different absorbance values at 405 nm. The results reported in Fig. 4B show that the temperature increases by about 0.5, 1.5, 4.2 and 7.1 °C at absorbance values (λ = 405 nm) of reference, 0.168, 0.036, and 0.336 units, respectively. A photothermal conversion efficiency value of η = 38.8 ± 2.8% with a time constant value of τ = 83 ± 19 s was calculated using Rope's equation as detailed in the SI. This value is similar to the photothermal conversion efficiency values calculated for analogous carbon dot nanostructures.

3.5 CDs–agar–PNM photophysical properties

CDs–agar–PNM exhibited interesting photophysical properties as photocatalytic and photothermal effects on blue light-excitation.[30] In particular, by absorbing UV-photons (300–400 nm), the carbon-sp^2 core of the nanostructures produces solvated electrons (e$^-$) and holes (h$^+$) through reaction (1), inducing photooxidation and photoreduction reactions, according to the the semiconductor band-gap value of 2.45 eV calculated using Tauc plot (Fig. 1A, insets),

$$\text{CDs–agar–PNM} + h\nu(300\text{ nm}) \rightarrow \text{CDs–gluc(h}^+) + \text{e}^- \qquad (1)$$

The photoreduction properties of CDs–agar–PNM were investigated by photochemical production of Au$^{(0)}$NPs through the following reactions:

$$\text{Au}^{\text{III}}\text{Cl}_4{}^- + 3\text{e}^- + n\ \text{CDs–agar–PNM} \rightarrow \text{CDs–agar–PNM/Au}^0\text{NPs} + 4\text{Cl}^- \qquad (2)$$

In detail, the photogenerated electrons (e$^-$) promote the reduction of Au$^{\text{III}}$ to Au^0, and the CDs–agar–PNM acts as a capping agent inducing the stabilization of the CDs–agar–PNM/Au^0 nanoparticles. Fig. 5 illustrates the optical absorption spectra of the CDs–agar–PNM/AuCl$_4{}^-$ dispersion after exposure to UV-light (2 lamps, 300 nm) at different irradiation times (0, 2, 4, 6, 8, 10, 20, 30, 45 and 60 min) under deaerated conditions. Under these conditions, the UV-photons are exclusively absorbed by the CDs–agar–PNM nanostructures. The appearance of the LSPR-band typical of AuNPs, centered at about 554 nm, confirmed the effective photoreduction of the Au$^{\text{III}}$ chloride precursor to Au^0 nanostructures. Furthermore, the photochemical process was confirmed by the experiments performed under dark conditions; in this case, no Au^0 nanostructure formation was observed, see Fig. S9. The inset in Fig. 5 shows the absorbance value at 554 nm for the irradiated (UV-light) and dark experiments at different irradiation times.

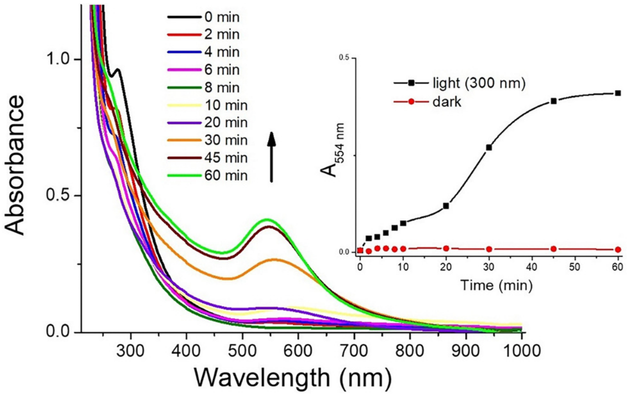

Fig. 5 Photoreduction experiments of CDs–agar–PNM: optical spectra changes of CDs–agar–PNM/gold precursor dispersion upon UV-light (300 nm) irradiation at different irradiation times. The inset shows the absorbance value at 554 nm upon irradiation (light 300 nm) and for dark conditions (no light).

3.6 Curcumin loading and thermal-induced release

To load curcumin into the CDs–agar–PNM nanosystem, excess of drug was added to the carbon dot water dispersion, and the mixture was stirred for 48 hours as described in the 3.1 section. Then, the sample was centrifuged to remove the unentrapped drug. The formation of the CDs–agar–PNM/curcumin adduct was confirmed using the spectroscopic method. The UV-vis absorption spectrum of CDs–agar–PNM/curcumin, reported in Fig. 6A, showed the typical curcumin absorption band at 433 nm and the typical π–π* band of the CDs at 275 nm. The curcumin loading was about 10%.

The thermally induced release of curcumin from the CDs–agar–PNM nanocontainer was spectroscopically investigated in water, see Fig. 6A. An efficient release of about 80% of curcumin was observed after just 5 min of incubation at 40 °C. Fig. 6B shows the curcumin release in terms of reduction of the absorbance value at 433 nm at different incubation times of 0, 2.5, 5, 10, 25, 25 and 35 min.

3.7 Biological experiments

Albumin is the most abundant protein in serum and exhibits nanocarrier properties to facilitate the targeted drug delivery by binding to receptors. It is well known that nonspecific interactions between protein and nanostructures occur in human fluids, resulting in the formation of the supramolecular protein–corona adduct. The formation of this supramolecular adduct reduces the association of nanostructures with other blood components, minimizing liver uptake and thus prolonging the nanoparticle circulation time in the bloodstream. This reduces the body's clearance of the nanostructures promoting the targeted delivery. Therefore, we decided to investigate the behaviour of CDs–agar–PNM nanostructures toward serum albumin (BSA) by steady-state fluorescence. To assess the interaction between CDs–agar–PNM nanostructures and BSA, steady-state fluorescence measurements were performed. The steady-state fluorescence intensity of BSA (4 mg mL^{-1}), using

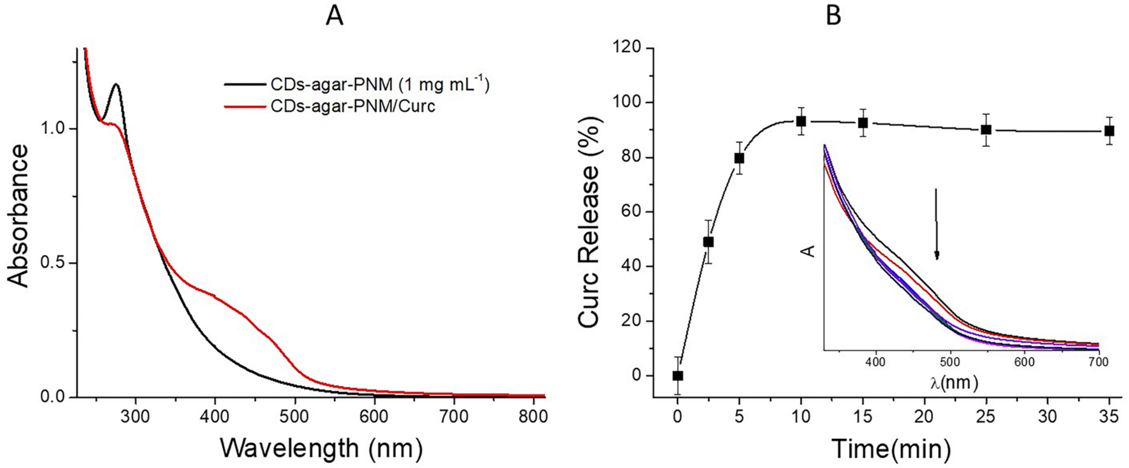

Fig. 6 CDs–agar–PNM/Curc: (A) optical absorption spectra of CDs–agar–PNM (black line) and CDs–agar–PNM/curcumin (red line) and (B) thermal-triggered release of curcumin from CDs–agar–PNM/curcumin (the insets show the optical absorption spectra at different incubation times).

an excitation wavelength of 280 nm in saline phosphate buffer (PBS), was quenched upon adding different concentrations of CDs–agar–PNM solutions (0.0, 0.048, 0.094, 0.14, 0.186, 0.23, 0.315, 0.403, 0.485, 0.565, and 0.642 mg mL^{-1}) without a shift of the maximum emission wavelength at 350 nm, Fig. 7A. Fluorescence quenching followed the well-known Stern–Volmer

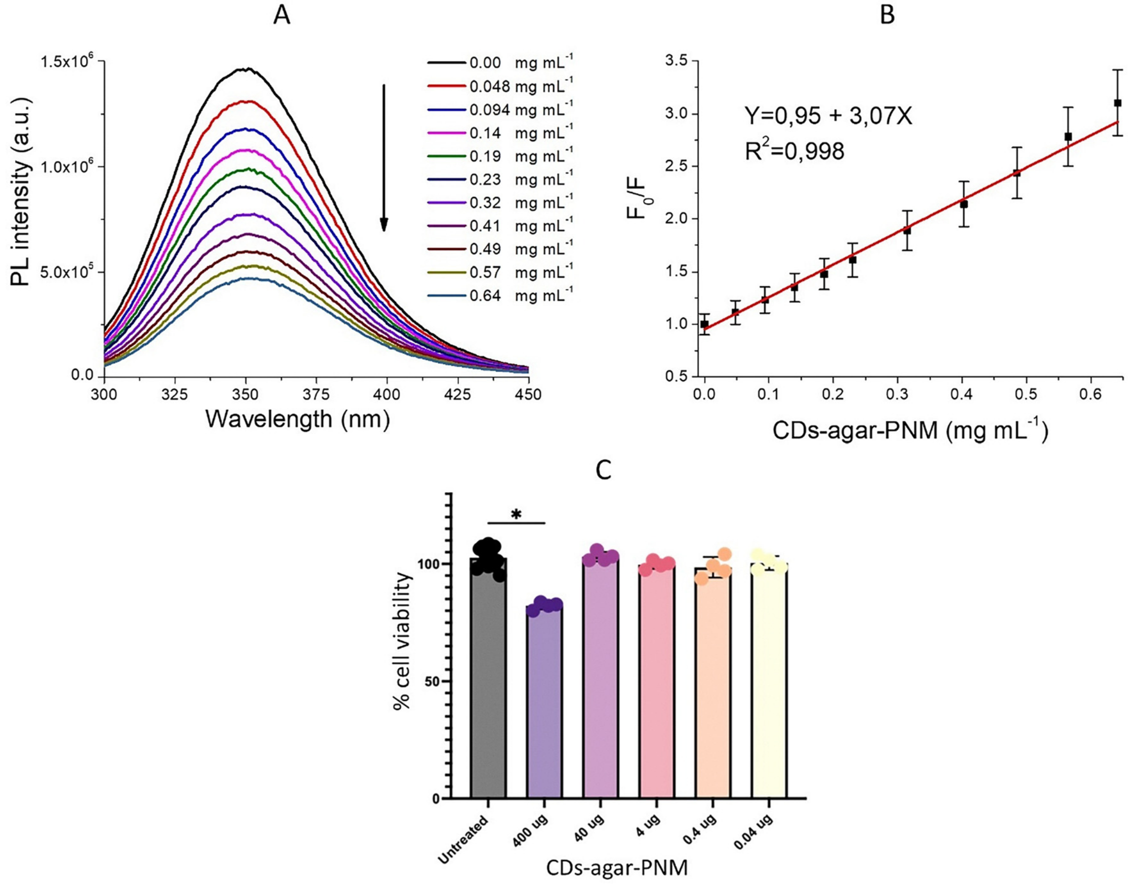

Fig. 7 Biological experiments: (A) fluorescence emission spectra of albumin at different concentrations of CDs–agar–PNM at 25 °C. The concentration of BSA is 4 mg mL^{-1}, and the CDs–agar–PNM concentrations for titration were 0.0, 0.048, 0.094, 0.14, 0.186, 0.23, 0.315, 0.403, 0.485, 0.565, and 0.642 mg mL^{-1}. (B) Stern–Volmer plots for the quenching of the fluorescence BSA by CDs–agar–PNM. (C) Toxicity tests on a human cell line. MTT assays of Caco-2 treated for 24 h with increasing concentrations of CDs–agar–PNM (400 μg μL^{-1}, 40 μg μL^{-1}, 4 μg μL^{-1}, 0.4 μg μL^{-1}, 0.04 μg μL^{-1}, and 0.004 μg μL^{-1}). Bars are means ± SEM of three independent experiments with n = 3.

equation expressed as follows:

$$\frac{F_0}{F} = 1 + k_q t_0[\mathrm{Q}] = 1 + K_{\mathrm{SV}}[\mathrm{Q}] \tag{3}$$

where F_0 and F are the fluorescence in the absence and presence of the quencher (carbon nanodots), respectively, [Q] is the carbon nanodot concentration, and K_{SV} is the Stern–Volmer constant, which indicates the quenching efficiency.[46] The result showed a K_{SV} value of 3.07 ± 0.3 ml mg^{-1}, see Fig. 7B.

3.8 Cytotoxicity experiments

The physicochemical properties of the CDs–agar–PNM, including the photothermal effect, the loading and the thermally controlled release of curcumin, were suitable for application as a drug delivery system, and therefore they stimulated us to investigate the biocompatibility of this novel nanocarrier. For this purpose, we exposed the human Caco-2 cell line to increasing concentrations of the nanostructures (400 μg μL^{-1}, 40 μg μL^{-1}, 4 μg μL^{-1}, 0.4 μg μL^{-1}, 0.04 μg μL^{-1}, and 0.004 μg μL^{-1}) for 24 h. At the end of the treatment, the viability of the cells treated with CDs–agar–PNM in the concentration range of 40–0.004 μg μL^{-1} was comparable to that of untreated controls (CTRLS) without remarkable effects on the cell morphology, while a slight increase in cytotoxicity of about 15% was observed at the highest nanostructure concentration of 400 μg μL^{-1}, see Fig. 7C.

3.9 Molecular dynamics simulations

To gain molecular-level insights into the conformational behavior of PNM and its interaction with agarose, atomistic molecular dynamics (MD) simulations were performed at different temperatures (305, 310, and 315 K). The main trends are summarized in Fig. 8, whereas complementary analyses and time-dependent plots are reported in the SI (Fig. S10–S16). Fig. 8A shows the evolution of the polymer radius of gyration for the different PNM lengths. A clear dependence on the chain size is observed. For the CDs–agar–PNM-24 system (blue line), the R_g decreases from about 16.5 Å to 9.5 Å after approximately 90 ns at 310 K, indicating a coil-to-globule transition. For the 32-mer (red line), a similar transition occurs later, after ∼130 ns, as the increased chain length delays compaction. The longest polymer, CDs–agar–PNM-40 (green line), remains in the coil state at 310 K, and the transition only takes place at 315 K after ∼150 ns of simulation. At 305 K, only minor fluctuations are detected, confirming the absence of conformational changes. Snapshots and extended trajectories supporting these results are provided in Fig. S10 and S11.

These observations are consistent with previous findings that hydrophilic surfaces, such as SiO_2, stabilize the coil conformation through hydrogen-bonding interactions that compete with polymer–solvent H-bonding.[32] Agarose behaves similarly: its hydroxyl groups interact strongly with the acceptor groups of PNM, stabilizing the coil form. Accordingly, a larger agarose–PNM interface (as in the 40-mer) increases the

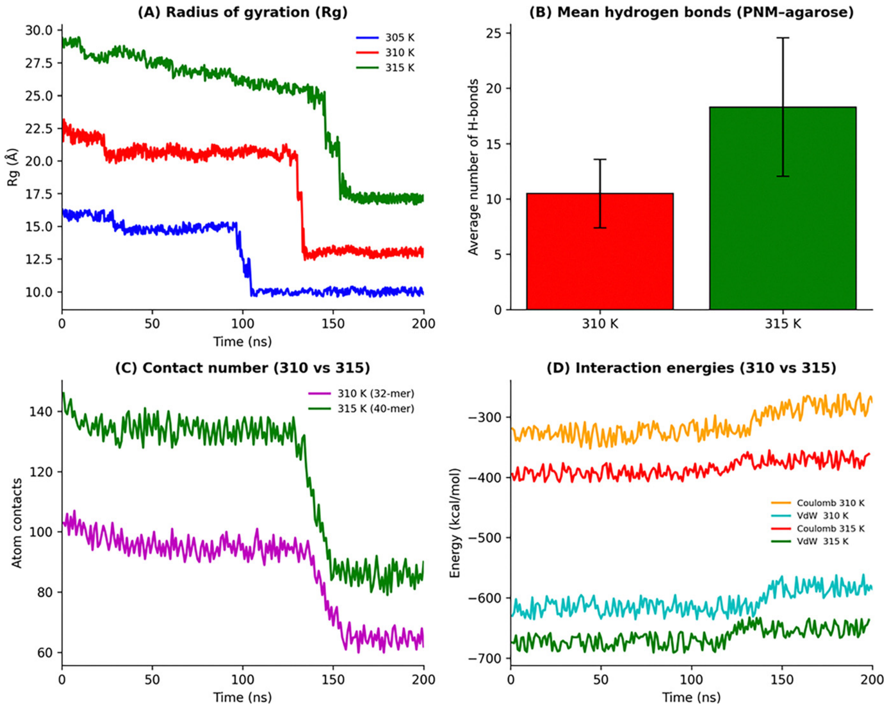

Fig. 8 Overview of molecular dynamics (MD) simulations for CDs–agar–PNM nanostructures at different temperatures. (A) Radius of gyration (R_g) of PNM chains (24-, 32-, and 40-mer) at 310 K and 315 K over 200 ns of simulation. (B) Average number of hydrogen bonds between agarose and PNM (32-mer) at 310 K and 315 K. (C) Contact number between agarose and the 32-mer and 40-mer PNM at 310 K and 315 K, respectively, showing the evolution of atomic contacts during the 200 ns trajectory. (D) Interaction energies between agarose and PNM 32-mer at 310 K and 40-mer at 315 K, with both coulombic and van der Waals (vdW) components.

transition temperature, whereas shorter chains undergo the transition more readily. To better understand the effect of PNM–agarose interactions, the contribution of hydrogen bonds between PNM and the polysaccharide was studied. Fig. 8B shows the average number of hydrogen bonds formed between 32- and 40-mer PNM and agarose at 310 K and 315 K. Both trajectories exhibit consistent mean values, confirming the reproducibility of the simulations and the stability of the polymer–agarose interactions. Detailed temperature-dependent analyses, Fig. S12, reveal that the reduction in the number of intermolecular hydrogen bonds coincides with the coil-to-globule transition identified from R_g. For instance, the decline in the H-bond count for PNM-24 occurs around 90 ns, whereas for PNM-32 and PNM-40, it appears at approximately 130 ns and 150 ns, respectively, matching the time evolution of R_g. In all cases, the transition takes place when the number of intermolecular hydrogen bonds drops below a threshold of ∼9–11, suggesting this range as a structural marker for conformational collapse.

The number of atomistic contacts between PNM and agarose (Fig. 8C) further supports this picture. At 315 K, the contact number is higher than that at 310 K, consistent with an enhanced interfacial association at elevated temperature. A contact is defined when any atom of PNM is within a distance of less than 0.4 nm from agarose. The decrease in the contact number observed during the simulations parallels the drop in R_g, indicating that the polymer detaches from the agarose surface as it collapses into a globule. Additional time-resolved contact maps for all simulated systems are presented in Fig. S13. The evolution of van der Waals and coulombic interaction energies between PNM and agarose is reported in Fig. 8D. Both energy components become more negative at 315 K, revealing stronger electrostatic and dispersive interactions. At 310 K, stable energy profiles indicate persistent adhesion for the longer chains (PNM-40), whereas at 315 K, a marked energetic minimum corresponds to the conformational transition. A full energetic decomposition by temperature and chain length is provided in Fig. S14. The effectiveness of hydrogen bonding was further examined using the autocorrelation function for PNM acceptor groups and hydrogen atom donors from the –OH groups on agarose. At 315 K and 310 K, *e.g.*, above the LCST of the investigated nanoparticles, the $c(t)$ curves exhibit a more rapid decay due to the globular conformation, which likely promotes the formation of intramolecular hydrogen bonds, Fig. S15. It is evident that above the LCST, the scale of H-bond persistence is in agreement with the radius of gyration results. In the same figure, the autocorrelation function at temperatures below the LCST displays a slower decay compared to that at higher temperatures, indicating that hydrogen bonds formed at 305 K are more persistent. Kinetic analysis suggests that the formation of hydrogen bonds between agarose and PNM stabilizes the coil conformation and is related to the polymer's extension.

Finally, the overall stability of the MD trajectories was evaluated through the root-mean-square displacement (RMSD) analysis, Fig. S16. RMSD values increase by approximately 1.5 Å during the simulations, reaching ∼4.1 Å at the end of the runs. The timing of these deviations—85 ns for the 24-mer, 135 ns for the 32-mer, and 150 ns for the 40-mer—aligns well with the R_g and H-bond trends. These computational findings qualitatively match the experimental observations from DLS, SEM, TEM and ^{1}H NMR spectroscopy. It should be noted that the discrepancies in the observed transition temperatures (>34 °C in the experimental data *versus* 37 °C and 40 °C in the simulated models) are largely attributable to the intrinsic limitations of the computational method, as well as to differences in the PNM/agarose ratios employed in the experiment compared to the simulated systems (MM ratio = 4560/7280 for 40-mer, 3636/7280 for 32-mer, and 2726/7280 for 24-mer).

4. Conclusions

In conclusion, this study successfully demonstrated the design and synthesis of a novel thermoresponsive nanocomposite, CDs–agar–PNM, which integrates carbon dots functionalized with agarose units covalently linked to poly(*N*-isopropylacrylamide) (PNM), for application in thermally controlled drug delivery. This three-component nanocomposite enabled efficient localized heating and precise modulation of the polymer's transition temperature, bringing it closer to physiological conditions. Comprehensive characterization using spectroscopic techniques, including UV-vis, NMR and ATR-FTIR, in conjunction with SEM and TEM imaging and DLS measurements, confirmed both the successful formation of the nanostructure and its thermoresponsive behavior. TEM and SEM analyses revealed the evolution from ∼7 nm carbon precursors to uniform spherical nanostructures of ∼200 nm after polymer functionalization, confirming the formation of a stable hybrid morphology. Notably, the nanocomposite exhibited a significant increase in LCST compared to unmodified PNM. The photothermal release of drug cargo based on coil-to-globule transition of PNM was clearly demonstrated and biocompatibility was validated *via* MTT assay. CDs–agar–PNM is a fascinating nanomaterial that, by combining the photoluminescence and photothermal properties of the carbon nanodots with the LCST functionality of the PNM, provides multiresponsive nanostructures. Molecular dynamics simulations further corroborated the experimental findings, revealing, furthermore, an LCST increase correlated with the PNM chain length. This was supported by an analysis of the radius of gyration, hydrogen bonding patterns, number of intermolecular contacts, and interaction energies between PNM and agarose. Overall, this work represents a significant advancement in the development of thermoresponsive drug delivery systems, demonstrating the tunability of LCST in PNM and highlighting the potential of the CDs–agar–PNM nanocomposite for biomedical applications, including hyperthermia-based therapies.

Author contributions

Salvatore Petralia: conceptualization, supervision, methodology, and writing – original draft. Ludovica Maugeri:

investigation. Nicolò Musso: investigation and editing. Grazia M. L. Consoli: investigation and editing. Giuseppe Consiglio: conceptualization and editing. Corinna Lombardo: investigation. Silvia Scalese: investigation and editing. Mario Scuderi: investigation and editing. Giuseppe Forte: conceptualization, supervision, methodology, and writing – original draft.

Conflicts of interest

The authors declare no conflicts of interest.

Data availability

The code for BIOVIA Discovery Studio can be found at **https://discover.3ds.com/discovery-studio-visualizer-download**. The revision of the code employed for this study is BIOVIA Material Studio 2017 (17.1.0.48).

The data supporting this article have been included as part of the supplementary information (SI). The supporting information file includes additional experimental data, spectroscopic characterizations, and computational analyses that complement the findings reported in the main manuscript. Specifically, it contains: molecular simulation models of the PNM–agarose–carbon dot system and representative snapshots from molecular dynamics trajectories (Fig. S1, S10). NMR characterizations, including ^{1}H, ^{13}C, and 2D-COSY spectra of agarose-, Cdots-agar-, and Cdots-agar–PNM-based materials in different solvents and temperatures (Fig. S2–S6). EDX elemental maps of CDs-agar and CDs-agar–PNM nanostructures (Fig. S7). DLS measurements of temperature-dependent hydrodynamic size variations of CDs-agar dispersions (Fig. S8). Optical absorption studies, including time-dependent spectra of CDs-agar–PNM/gold precursor solutions (Fig. S9). Computational analyses, including radius of gyration trends, hydrogen-bond counts, atom–atom contact analyses, interaction energy profiles, and autocorrelation functions obtained from MD simulations at different temperatures (Fig. S11–S15). Cytotoxicity results and statistical analyses (Table S1).NMR chemical shift assignments for Cdots-agar at elevated temperature (Table S2). Photothermal conversion efficiency data, including equations used, experimental conditions, raw data, and fitted parameters (Table S2 and Fig. S4). Together, these data provide additional structural, spectroscopic, thermal, and biological information supporting the synthesis, characterization, and functional evaluation of the CDs-agar–PNM nanomaterials. See DOI: **https://doi.org/10.1039/d5tb01844g**.

Acknowledgements

This work has been partially funded by the European Union (NextGenerationEU), through the National Centre for HPC, Big Data and Quantum Computing (E63C22001000006) and by Linea di Intervento 1 – Progetti di Ricerca Collaborativa del "PIAno di inCEntivi per la RIcerca di Ateneo 2024/2026" (University of Catania). Title Project: MhyNano: Multifunctional hybrid nanomaterials for cancer diagnosis and personalized targeted therapy. Scanning electron microscopy characterization was supported by the facility provided by "Nano Foundries and Fine Analysis – Digital Infrastructure (NFFA-DI)" – CUP: B53C22004310006, within the Piano Nazionale di Ripresa e Resilienza (PNRR) – Italian National Recovery and Resilience Plan. Transmission electron microscopy characterization was carried out using the facilities provided by the Italian Infrastructure Beyond-Nano UPGRADE – Materials and processes Beyond the Nano-scale (DFM.AD006.173) – CUP: DFM.AD006.173 funded by Consiglio Nazionale delle Ricerche (CNR) – Dipartimento "Scienze fisiche e tecnologie della materia". The authors are grateful to Dr F. Benevelli (Bruker Biospin srl Milano) for technical assistance in performing NMR and ^{13}C NMR spectroscopy.

References

1 D. Ghosh Dastidar and G. Chakrabarti, Thermoresponsive Drug Delivery Systems, Characterization and Application, *Applications of Targeted Nano Drugs and Delivery Systems Nanoscience and Nanotechnology in Drug Delivery Micro and Nano Technologies*, 2019, pp. 133–155.
2 F. L. Lopez, T. B. Ernest, C. Tuleu and M. O. Gul, *Expert Opin. Drug Delivery*, 2015, **12**(11), 1727–1740.
3 D. J. McClements, *Adv. Colloid Interface Sci.*, 2015, **219**, 27–53.
4 A. S. Kulshrestha and A. Mahapatro, *ACS Symp. Ser.*, 2008, 1–7.
5 U. D. Bret, N. S. Lakshmi and C. T. Laurencin, *J. Polym. Sci., Part B: Polym. Phys.*, 2011, **3**(49), 832–864.
6 R. Coronado, S. Pekerar, A. T. Lorenzo and M. A. Sabino, *Polym. Bull.*, 2011, **67**(1), 101–124.
7 C. B. P. Oliveira, V. Gomes, P. M. T. Ferreira, J. A. Martins and P. J. Jervis, *Gels*, 2022, **8**(11), 706.
8 S. Rasib, Z. Ahmad, A. Khan, H. Akil, M. Othman, Z. Hamid and F. Ullah, *Int. J. Biol. Macromol.*, 2018, **108**, 367–375.
9 M. Heskins and J. E. Guillet, *J. Macromol. Sci., Chem.*, 1968, **2**(8), 1441–1455.
10 H. G. Schild, *Prog. Polym. Sci.*, 1992, **17**, 163–249.
11 E. I. Tiktopulo, V. N. Uversky, V. B. Lushchik, S. I. Klenin, V. E. Bychkova and O. B. Ptitsyn, *Macromolecules*, 1995, **28**, 7519–7524.
12 K. Kubota, S. Fujishige and I. Ando, *J. Phys. Chem.*, 1990, **94**, 5154–5158.
13 X. Wang, X. Qiu and C. Wu, *Macromolecules*, 1998, **31**, 2972–2976.
14 C. Wu and X. Wang, *Phys. Rev. Lett.*, 1998, **18**, 4092–4094.
15 Y. Maeda and M. Yamabe, *Polymer*, 2009, **50**(2), 519–523.
16 A. J. Convertine, B. S. Lokitz, Y. Vasileva, L. J. Myrick, C. W. Scales, A. B. Lowe and C. L. McCormick, *Macromolecules*, 2006, **39**(5), 1724–1730.
17 X. Zhang, B. H. Tan and C. He, *Macromol. Rapid Commun.*, 2013, **34**(22), 1761–1766.
18 T. E. de Oliveira, D. Mukherji, K. Kremer and P. A. Netz, *J. Chem. Phys.*, 2017, **146**(3), 034904.

19 X. Yin, A. S. Hoffman and P. S. Stayton, *Biomacromolecules*, 2006, **7**(5), 1381–1385.

20 G. Damonte, M. Cozzani, D. Di Lisa, L. Pastorino, A. Mariani and O. Monticelli, *Eur. Polym. J.*, 2023, **195**, 112239.

21 A. Trubetskaya, J. Leppiniemi, S. Lipponen, S. Lombardo, W. Thielemans, T. Maloney, T. Pääkkönen, K. K. Kesari, J. Ruokolainen, V. P. Hytönen and E. Kontturri, *Mater. Adv.*, 2024, **5**, 570–583.

22 G. Conzatti, C. Nadal, J. Berthelot, L. Vachoud, M.-N. Labour, A. Tourette and E. Belamie, *ACS Appl. Bio Mater.*, 2024, **7**(5), 3033–3049.

23 B. Garcia-Pinel, A. Ortega-Rodriguez, C. Porras-Alcalà, L. Cabeza, R. Contreras-Cáceres, R. Ortiz, A. Diaz, A. Moscoso, F. Sarabia, J. Prados, J. M. López-Moreno and C. Melguizo, *Artif. Cells, Nanomed., Biotechnol.*, 2020, **48**(1), 1022–1035.

24 S. M. Khodadadi Yazdi, A. Taghizadeh, M. Taghizadeh, F. J. Stadler, M. Farokhi, F. Mottaghitalab, P. Zarrintaj, J. D. Ramsey, F. Seidi, M. R. Saeb and M. Mozafari, *J. Controlled Release*, 2020, **326**, 523–543.

25 G. Forte, G. Ventimiglia, M. Pesaturo and S. Petralia, *Biotechnol. J.*, 2022, **17**(6), e2100587.

26 A. M. El-Kady, A. A. Ali and A. El-Fiqi, *J. Non-Cryst. Solids*, 2020, **534**, 119889.

27 F. Ghanbari Adivi, P. Hashemi and A. Dadkhah Tehrani, *Polym. Bull.*, 2019, **76**(3), 1239–1256.

28 C. Kim, D. Jeong, S. Kim, Y. Kim and S. Jung, *Carbohydr. Polym.*, 2019, **222**, 115011.

29 L. Maugeri, G. Fangano, E. Butera, G. Forte, P. G. Bonacci, N. Musso, F. Ruffino, L. Ferreri, G. M. L. Consoli and S. Petralia, *Pharmaceutics*, 2025, **17**(5), 543.

30 N. Musso, P. G. Bonacci, G. M. L. Consoli, L. Maugeri, M. Terrana, L. Lanzanò, E. Longo, G. Buscarino, A. Consoli and S. Petralia, *J. Colloid Interface Sci.*, 2025, **696**, 137873.

31 S. M. Hosseini, J. Mohammadnejad, R. Najafi-Taher, Z. B. Zadeh, M. Tanhaei and S. Ramakrishna, *ACS Appl. Bio Mater.*, 2023, **6**(4), 1323–1338.

32 G. Consiglio and G. Forte, *Phys. Chem. Chem. Phys.*, 2018, **20**, 29754–29763.

33 G. M. L. Consoli, M. L. Giuffrida, C. Satriano, T. Musumeci, G. Forte and S. Petralia, *Chem. Commun.*, 2022, **58**(19), 3126–3129.

34 G. Forte, G. Consiglio, C. Satriano, L. Maugeri and S. Petralia, *Colloids Surf., B*, 2022, **217**, 112628.

35 G. M. L. Consoli, M. L. Giuffrida, S. Zimbone, L. Ferreri, L. Maugeri, M. Palmieri, C. Satriano, G. Forte and S. Petralia, *ACS Appl. Mater. Interfaces*, 2023, **15**(4), 5732–5743.

36 G. M. L. Consoli, L. Maugeri, G. Forte, G. Buscarino, A. Gulino, L. Lanzanò, P. Bonacci, N. Musso and S. Petralia, *J. Mater. Chem. B*, 2024, **12**, 952–961.

37 G. M. L. Consoli, G. Forte, L. Maugeri and S. Petralia, *ChemPhotoChem*, 2024, e202400088.

38 G. M. L. Consoli, L. Maugeri, N. Musso, A. Gulino, L. D'Urso, P. Bonacci, G. Buscarino, G. Forte and S. Petralia, *Adv. Healthcare Mater.*, 2024, **13**(16), 2303692.

39 J. T. Margraf, V. Strauss, D. M. Guldi and T. Clark, *J. Phys. Chem. B*, 2015, **119**(24), 7258–7265.

40 S. A. Deshmukh, S. K. R. S. Sankaranarayanan, K. Suthar and D. C. Mancini, *J. Phys. Chem. B*, 2012, **116**, 2651–2663.

41 L. Fritz and D. Hofmann, *Polymer*, 2012, **38**, 1035–1045.

42 S. A. Deshmukh, Z. Li, G. Kamath, K. J. Suthar, S. K. R. S. Sankaranarayanana and D. C. Mancini, *Polymer*, 2013, **54**, 210–222.

43 S. A. Deshmukh, S. K. R. S. Sankaranarayanana and D. C. Mancini, *J. Phys. Chem. B*, 2012, **116**, 5501–5515.

44 A. Luzar and D. Chandler, *Nature*, 1996, **379**, 55–57.

45 A. Philippidis, A. Spyros, D. Anglos, A. B. Bourlinos, R. Zbořil and E. P. Giannelis, *J. Nanopart. Res.*, 2013, **15**, 1777.

46 G. M. L. Consoli, L. Maugeri, G. Forte, D. Bongiorno, E. Nicitra, D. Aleo, F. Spitaleri, L. Ferreri, G. Buscarino, T. Campagna, N. Musso and S. Petralia, *ACS Appl. Nano Mater.*, 2025, **8**(2), 1078–1090.